JOURNAL OF SPACECRAFT AND ROCKETS
Vol. 39, No. 1, January–February 2002

Design of a Hybrid Chemical/Electric Propulsion Orbital Transfer Vehicle

Laurie M. Mailhe* and Stephen D. Heister†
Purdue University, West Lafayette, Indiana 47907-1282

A hybrid chemical/electric propulsion orbital transfer vehicle was studied for a coplanar transfer from low Earth orbit to geosynchronous orbit. The goal of this study was to develop a strategy combining the two propulsion systems to reduce total radiation loads on the spacecraft and to provide attractive total trip times. Propulsion systems were sized based on current technology storable bipropellants for the chemical stage; three separate electric propulsion systems were considered for the low-thrust portion of the mission. The effect of the relative amounts of chemical propulsion on trip time, vehicle mass, and overall radiation dosage has been characterized. In addition, the effect of orbit inclination, the altitude for initiation of the chemical propulsive burns, and payload mass have been considered. Attractive options have been identified that are substantially lighter than a pure chemical system and that offer trip times and radiation loads substantially less than a pure electric system.

Nomenclature

a	=	spacecraft's acceleration, km/s^2
E	=	particle energy, MeV
F	=	thrust, N
I_{sp}	=	specific impulse, s
i	=	orbit inclination, rad
L_{shell}	=	L shell in Earth radii
m	=	mass, kg
$\dot{m}$	=	mass-flow rate, kg/s
P_w	=	total input power, kW
r	=	position radius from Earth's center, km
r_e	=	distance in Earth radii
t	=	time, s
β	=	specific mass, kg/kW
γ	=	flight-path angle, rad
ΔV	=	delta V, km/s
η	=	efficiency
θ	=	argument of latitude, rad
λ	=	magnetic latitude, rad
μ	=	Earth gravitational constant, 3.986×10^5 km^3/s^2
Φ	=	particle flux, particles/cm^2/s

Indices

pp	=	power processor
R	=	radiator
T	=	total
th	=	thruster/thermal
tpp	=	system thruster/power processing unit

Introduction

UPPER-STAGE systems are performance driven because they must be carried to low Earth orbit (LEO). For this reason, low-thrust electric propulsion devices provide an attractive alternative to traditional chemical propulsion upper-stage systems. The advent of new high-power arcjet and Hall effect thruster (HET) devices, combined with significant efficiency gains in solar voltaic technologies, has made electric propulsion a viable alternative for this application.[1,2] Many studies on orbital transfer from LEO to geosynchronous orbit (GEO), involving electric propulsion have been performed.[3–8] In the case of orbit transfer, the use of electric thrusters as primary propulsion leads to a significant increase in total trip time. Accordingly, earlier efforts were mainly focused on optimization of the trajectory to minimize the total trip time or the total fuel consumption.[6–8] One of the main issues/concerns associated with all-electric orbital transfers is the potential radiation dose due to extended times required to traverse the Van Allen radiation belts.

A dual high/low thrust (chemical/electric propulsion) is a viable alternative to reduce radiation exposure in missions where this is a concern. A high-thrust chemical propulsion system would be utilized to rapidly traverse high-radiation zones in the Van Allen belts and the higher efficiency low-thrust electric propulsion system would then be used for the remainder of the mission. Several studies have been performed on combined chemical/electric propulsion trajectories. Early work[9] showed that the use of high thrust and low thrust combined is often superior in payload capability to the use of either system alone for a high change in radius. Other works[10,11] have shown the desirability of this option for lunar and interplanetary missions.

In the present study, a combined high-thrust/low-thrust orbital transfer vehicle is used to simulate a coplanar LEO to GEO transfer. The goal of this work is to evaluate the influence of the payload mass, the engine type, the initial altitude for the application of a high-thrust system, and the inclination of the orbit. Their effects on the total trip time, the radiation level, and the gross weight of the vehicle are analyzed. The following sections describe the elements and validation of the model, results, and conclusions from this study.

Model Development

The overall model has four major components: propulsion design, trajectory integration, radiation calculations, and mission design. This level of detail permits investigation of tradeoffs between the propulsion system, the integrated radiation dose, and the selected trajectory/mission design. The propulsion system design is further subdivided into two classes, the high-thrust chemical propulsion system and the low-thrust electric propulsion system. The following subsections briefly outline the sizing/design methodology employed in each of these modules; a more detailed discussion can be found in Ref. 12. Here, our goal is to provide propulsion design algorithms suitable for parametric studies. For this reason, the techniques may not replicate weights for actual thrusters, but will vary in a physically realistic manner with changes in engine thrust.

Propulsion System Design

High-Thrust Chemical Propulsion System Design

The chemical propulsion design is based on the technology level employed in the space shuttle orbital maneuvering system (OMS) engine.[13] This engine utilizes storable liquid hypergolic propellants: nitrogen tetroxide (N_2O_4) and monomethyl hydrazine (MMH) with

Received 26 June 2000; revision received 5 July 2001; accepted for publication 18 July 2001.

*Graduate Research Assistant, School of Aeronautics and Astronautics.
†Professor, School of Aeronautics and Astronautics, 1282 Grissom Hall. Associate Fellow AIAA.

Table 1 Space shuttle OMS performance in vacuum

Parameter	Value
Thrust	26,700 N
Specific impulse	313.2 s
Chamber pressure	862 kPa
Mass-flow rate	8.61 kg/s
Expansion ratio	55
Thrust coefficient	1.81

a mixture ratio of 1.65. This engine has performance similar to that of numerous other space engines using N2O4/MMH propellants and was viewed as a reasonable alternative for moderate-sized payloads. Table 1 provides a summary of performance characteristics for this engine.

Components that are sized in this design module include the thrust chamber, injector, nozzle, propellant tanks, and pressurant tank. Miscellaneous components such as valves, plumbing, and regulators are budgeted 5% of the propellant mass in the system. The design methodologies employed follow guidelines set by Humble et al.[14] Propellant tanks are sized assuming an 8% ullage volume to allow for trapped propellant and possible propellant expansion under high-temperature conditions. Tanks are assumed to be spherical and of titanium construction with a tank design factor of the design burst pressure times the internal volume, divided by the tank weight (PV/W) (a top-level performance measure for a pressure vessel) of 2500 m (Ref. 14). Tanks are designed with a structural factor of safety of 1.25, and the tank pressure is assumed to be 25% higher than the chamber pressure (Table 1) to provide an adequate pressure drop for injector performance.

Titanium is also utilized for the pressurant tank, and a PV/W of 6350 m is assumed.[15] Helium pressurant is utilized at an initial pressure of 21 MPa with a final pressure equivalent to the tank pressure. The pressurant is assumed to begin at room temperature (273 K), and an adiabatic blowdown process is assumed to determine gas temperature during the firing process and the total amount of pressurant required. To determine the total volume of pressurant required, an iterative method is applied because the pressurant tank volume itself is initially unknown. Iteration on the pressurant tank volume proceeds until adequate pressurant is available to fill all three tanks (fuel, oxidizer, and pressurant) with gas at the selected tank pressure.

The combustion chamber is sized using the methodology described in Ref. 14, wherein wall thicknesses are determined from thin-walled pressure vessel theory. The chamber throat area is determined from Table 1 information, and the chamber internal diameter is computed from a correlation in Ref. 14. The chamber length is derived from combustion residence time considerations.[14] Columbium is assumed as the chamber material; it has a density and ultimate tensile strength of 8500 kg/m^3 and 310 MPa, respectively. Here, a safety factor of 2.5 was utilized to account for stress concentrations developed from the high-temperature combustion gases. The design burst pressure was assumed to be 25% greater than the chamber pressure, and the injector was assumed to be a plate of thickness twice that of the chamber. The nozzle was assumed to be columbium as well and was designed assuming a 15-deg conical shape. Note that the exit diameter can be computed from the throat area and expansion ratio.

Low-Thrust Electric Propulsion System Design

The electric propulsion system comprises a solar array power source, propellant tankage, thrusters, a power processing unit, and radiators for rejection of excess heat. Three different low-thrust engines are implemented in the model: a 30-kW arcjet based on the electric propulsion space experiment (ESEX) engine,[16] a stationary plasma thruster (SPT-100)[17] and an HET-220 are studied.[18] For practical design reasons, it was decided that a number of four thrusters was a maximum. For each engine, the set of inputs in Table 2 is given.

The SPT-100 and HET-220 uses xenon as propellant, whereas ammonia is used for the ESEX thruster. Xenon propellant is stored as a supercritical gas at 74-MPa pressure. Ammonia is stored as a saturated liquid at pressure of 1.4 MPa (Ref. 19). The titanium tanks

Table 2 Characteristics of electric thrusters used in the study

Thruster	Power, kW	Thrust, mN	I_{sp}, s	η_{th}, %	η_{pp}, %	Mass flow, mg/s	Number of thrusters
SPT-100	5.4	332	1600	50	96.5	20.4	4
ESEX 30-kW arcjet	26	1930	787	28.4	95	240	1
HET-220	43	2096	2379	57	95	89.6	4

are assumed to be spherical and are sized using thin-walled pressure vessel theory with a safety factor of 1.25.

The engines are all assumed to be powered by solar arrays. Although arrays using gallium arsenide cells are less sensitive to radiation degradation than the traditional silicon photovoltaics, they tend to be heavier [specific mass of 16.7 kg/kW vs 7.2 kg/kW for Si (Ref. 20)]. The choice was made for the lightest one because the radiation dose is to be minimized as a result of the mission strategy. Thus, the solar array mass is simply the product of the specific mass and the selected power level. A power processing unit (PPU) transforms the array output into the form suitable for the thruster. Following Ref. 14, the system thruster/PPU specific mass (kilograms per kilowatt) β_{tpp} is modeled as a function of the specific impulse I_{sp}:

$$\beta_{tpp} = C \cdot I_{sp}^{D} \tag{1}$$

where β_{tpp} is in units of kilograms per kilowatt. The parameters C and D had values of 1.8 and 0.0 for the arcjet thruster,[14] and a C value of 123,100 and D value of -1.198 were used for the other two thrusters. Engine and PPU masses were obtained by multiplying β_{tpp} by the selected power level.

Although the thrusters employed are generally assumed to radiate excess power during operation, radiators were sized for the spacecraft assuming that one would want to make use of the large power available from the solar arrays once in orbit. A specific radiator mass of 4 kg/kW was assumed in this instance to budget mass for the radiators for this purpose.

Radiation Belt Modeling

The doughnut-shaped Van Allen belts are most prominent at latitudes less than about 60° and at midaltitude regions between LEO and GEO. The inner belt occupies a compact region above the geomagnetic equator (3000–25,000-km altitude). It is populated by protons of energies in the 10–100-MeV range. The outer belt is nowadays seen as part of the plasma population, for example, ions of about 1 MeV of energy.

Modeling the complex phenomena of the space radiation environment is not a straightforward task. Indeed, solar proton events and cosmic rays greatly influence the dynamics of the belts. The model utilized in this study is derived from Ref. 19 and assumes a minimum solar activity and no cosmic rays events. Radiation levels are presumed to be constant on torroidal surfaces denoted by an L-shell value. A magnetic L shell is the surface generated by rotating a magnetic field line around the dipole axis as illustrated in Fig. 1. The magnetic L-shell surface approximately satisfies

$$L_{shell} = r_e \Big/ \cos^2(\lambda) \tag{2}$$

where r_e is the distance from the Earth's center expressed in Earth radii and λ is the magnetic latitude.[19] The axis of the magnetic field is tipped with respect to the rotation axis of the Earth by 11.4 deg. Therefore, true north, which is defined by the direction to the north rotational pole, does not coincide with the magnetic north, which is defined by the direction to the north magnetic pole. However, they are assumed identical in this model, and the magnetic latitude is defined by the following equation:

$$\lambda = \arcsin[\sin(\theta) \cdot \sin(i)] \tag{3}$$

The magnetic latitude is a function of the spacecraft's argument of latitude θ and the orbit inclination i. Note that the longitude of the ascending node is assumed to be zero. Fluxes for electrons with energies higher than 0.5 MeV and protons with energies higher than

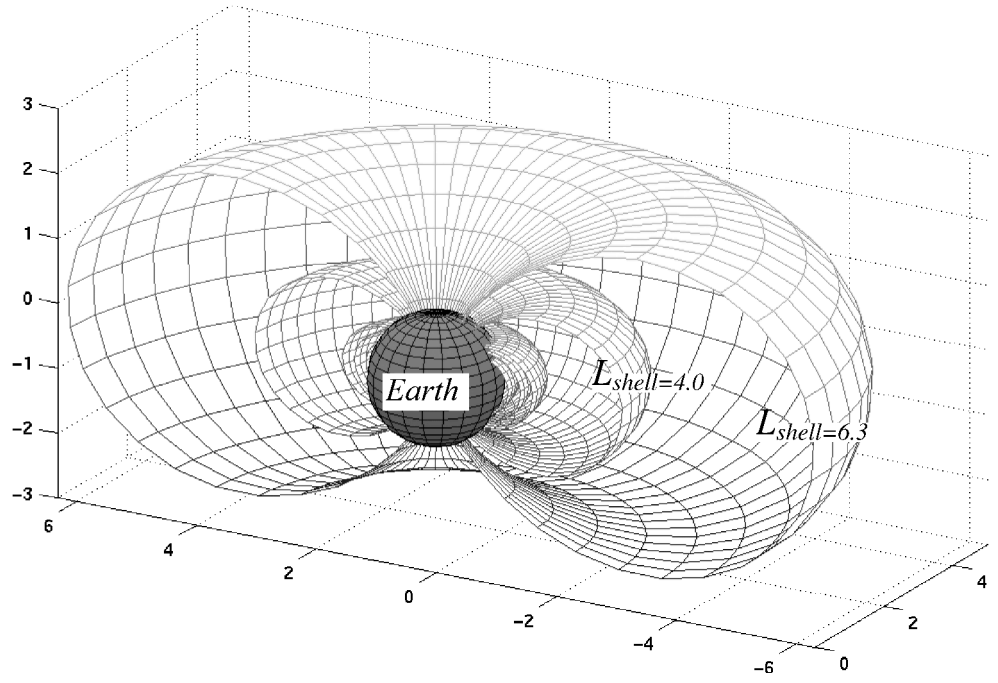

Fig. 1 Van Allen radiation belts schematic using L_{shell} model. (Radiation levels are assumed to be constant on each L-shell contour.)

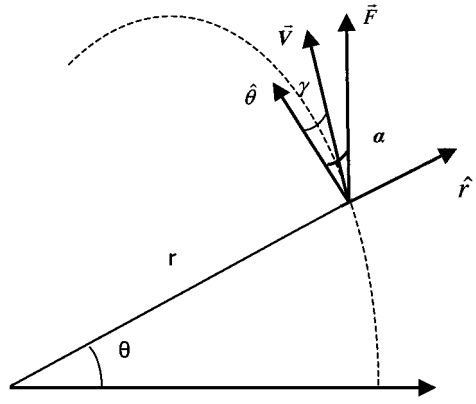

Fig. 2 Definition of the trajectory in a coordinate system with origin at the Earth's center.

100 MeV are computed on surfaces of constant L-shell values. If the magnetic latitude is higher than 60°, the radiation is negligible. This total energy flux integrated for each step time along the trajectory gives the total radiation dose for a given mission. A more detailed description of the radiation environment (including solar activity and cosmic rays) can be found in Refs. 20–23.

Trajectory Model: Mission Design

In deriving the spacecraft's equations of motion, a simple spherical gravitational field without any perturbations due to solar radiation pressure, third-body effects, or other small forces is assumed. Constant thrust is assumed during all propulsive burns and a planar trajectory is considered for all cases.

The Earth-centered spherical $(\hat{r}, \hat{\theta})$ coordinate system used in the study is shown in Fig. 2. The vector $\boldsymbol{F}$ represents the thrust vector and α the thrust angle. The velocity $\boldsymbol{V}$ makes an angle γ called the flight-path angle with the normal direction. The thrust is assumed to be parallel with the velocity vector. It is well known that this condition is an optimum direction for very low continuous thrust transfer.[24] This approximation is also employed for chemical propulsion burns. Under these assumptions, the equations of motion are

$$\dot{r}(t) = \dot{r} = u \tag{4}$$

$$\dot{\theta}(t) = \dot{\theta} = v/r \tag{5}$$

$$\dot{u}(t) = \ddot{r} = v^2/r - \mu/r^2 + a\sin\alpha \tag{6}$$

$$\dot{v}(t) = r\ddot{\theta} + r\dot{\theta} = -[(u \cdot v)/r] + a\cos\alpha \tag{7}$$

where μ is the Earth gravitational constant, that is, 3.986×10^5 km^3/s^2; r is the radius; θ is the argument of latitude or position angle; u is the radial velocity; and v is the normal velocity. The spacecraft's acceleration magnitude a and the thrust angle α are defined as

$$a(t) = F/(m_0 - \dot{m} \cdot t) \tag{8}$$

$$\sin(\gamma) = u\Big/\sqrt{u^2 + v^2} \tag{9}$$

where m_0 is the spacecraft mass at the start of the firing and $\dot{m}$ is the propellant mass-flow rate during thruster operation. Once the propulsion mass budget is defined from the estimated propellant load and the initial engine characteristics (i.e., mass-flow rate and thrust level) chosen, the integration of the trajectory is initiated. The state variables initial values correspond to a circular orbit at an altitude of about 200 km (LEO), whereas the end state was assumed to be a circular orbit at geosynchronous altitude. Under these assumptions, the initial conditions for the trajectory integration were

$$r(t_0) = 6578 \text{ km}, \qquad u(t_0) = 0 \text{ km} \cdot \text{s}^{-1}$$

$$v(t_0) = \sqrt{\mu/r_0} = 7.784 \text{ km} \cdot \text{s}^{-1}, \qquad a(t_0) = F/m_0$$

The equations of motion (4–7) are integrated using a fourth-order fixed-step Runge–Kutta numerical integration scheme until the desired final radius of 42,164 km was attained.

The simulation allows for four different mission strategies: 1) all low thrust (L), 2) high thrust/low thrust (H/L), 3) low thrust/high thrust/low thrust (L/H/L), and 4) all high thrust (H). Note that the solar arrays and antenna must be stored before high thrust burns, and so the L/H/L strategy would require a deployment/storage/deployment of solar arrays. The switch from low thrust to high thrust is performed at a chosen radius (R_{switch}). This radius is to be optimized on consideration of the Van Allen radiation belts.

The high-thrust portion of the mission is based on a Hohmann transfer with two burns and a coast phase as shown in a typical trajectory plot in Fig. 3. However, because real engines are considered,

the burns are not impulsive and are smeared over a small arclength of the trajectory, thereby leading to a small gravity loss during this flight segment. For a typical burn time of 150 s, a radius change of about 5 km and an angle change of about 8 deg are observed. It has been shown[25] that burns centered on the line of apsides produce behavior equivalent to an ideal Hohmann transfer. This approach was not practical in this analysis due to changes in vehicle mass during the burn and the implicit nature of such a requirement. For this reason, the second thrust burn (TB2) is initiated when the flight-path angle is smaller than 10^{-3} deg after the first thrust burn (TB1). This condition proved to provide an adequate replication of the Hohmann transfer.[12]

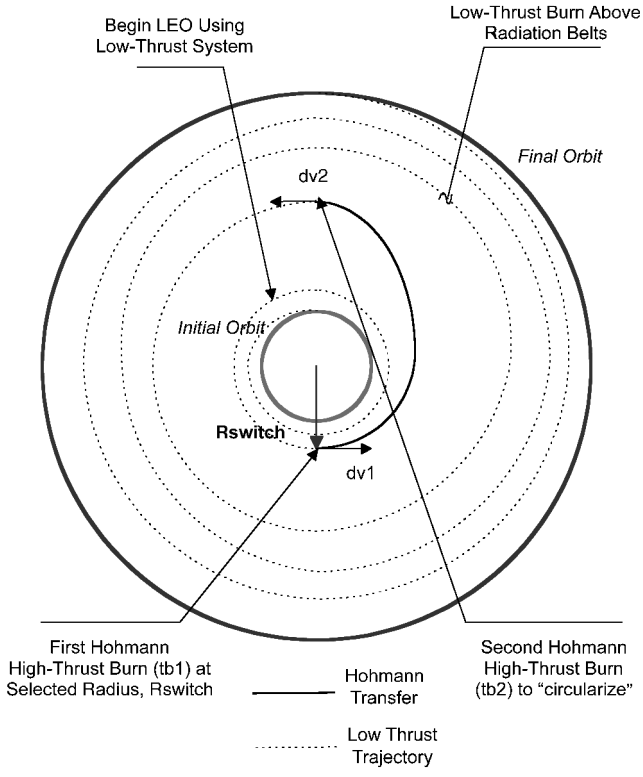

Fig. 3 Schematic of the different phases of the mission; the radius R_{switch} denotes the location where high-thrust chemical propulsion is initiated.

One of the requirements for the mission is that the flight-path angle at arrival be as close as possible to zero. This requirement will minimize any correction maneuver when reaching the final orbit. The second burn time in the Hohmann maneuver (TB2) is optimized such that the flight-path angle at arrival is below 1 deg. Changes in TB2 reflect nonlinear effects because vehicle propulsion masses are adjusted to accommodate varying amounts of propellant consistent with this parameter. For this reason, the flight-path angle at arrival is not a monotonic function with respect to the second burn time. For each TB2, the final radius slightly differs from 42,164 km and the computed flight-path angle corresponds then to a slightly different orbit and different vehicle. Figure 4 depicts these trends for a given trajectory and vehicle design strategy. Results indicate an optimal TB2/TB1 ratio, referred as TB2*, to minimize the flight-path angle at arrival. The TB2 value minimizing the flight-path angle was found for three values of TB1: 50, 100, and 150 s. The three data points were curve fitted to provide an optimal TB2 value for an arbitrary TB1 in this range. This strategy provided a means to minimize flight-path angles at arrival for all cases employing the high-thrust propulsion before a low-thrust burn.

To get the exact propellant loading on the spacecraft, an iteration is completed for the low-thrust propellant mass. The high-thrust propellant load is fully determined by the two burn times and the given mass-flow rate. An initial guess gives the spacecraft's initial inert mass design. The mission is run, and the actual low-thrust propellant burnt during the mission is compared to the initial load. If they do not match within 0.1% of the mass burnt, the initial load is updated to half of the sum of the previous initial mass and the actual used mass, and a new design of the propulsion system is done accordingly. To not burden the spacecraft with a useless payload, the high-thrust inert mass is jettisoned after the second burn. Only the first mission has an arbitrary initial guess. After convergence of the mass iteration for the given mission, that is, TB1, the next initial guess is for the new mission is the preceding step solution. This increases the convergence rate on the propellant mass iteration. The very first run takes about 13 iterations to converge within 0.1%, whereas subsequent runs take four to five iterations to reach the same accuracy.

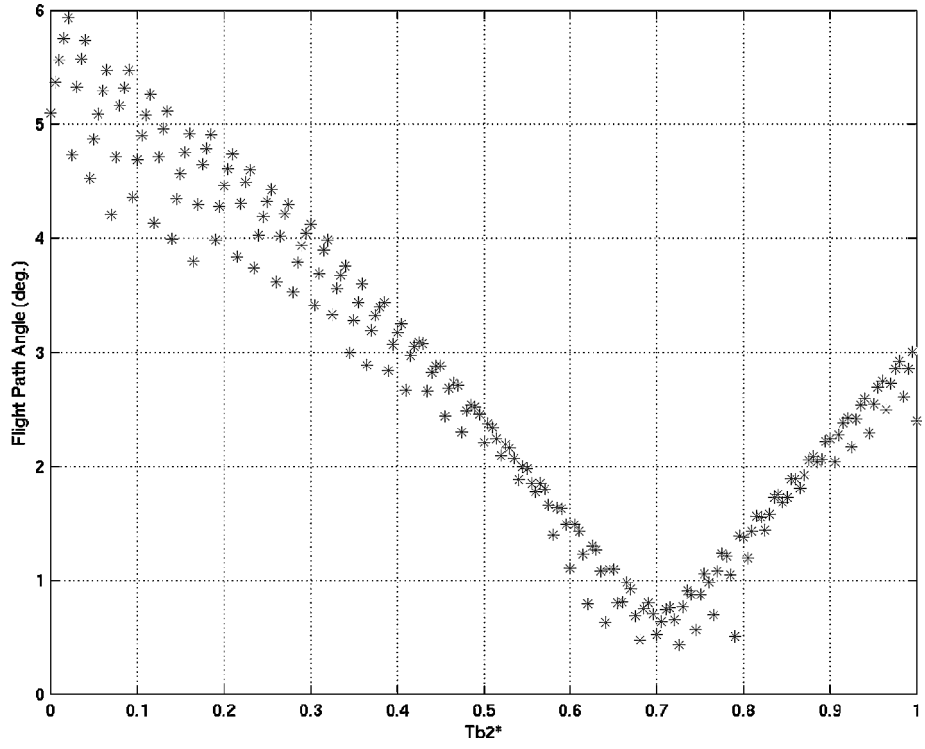

Fig. 4 Flight-path angle vs TB2* for TB1 = 100 s; an optimal TB2 value exists to minimize the flight-path angle at arrival.

Model Validation

Propulsion sizing modules were validated by comparison with hand calculations for a baseline case described in the following section. In addition, propulsion system mass fractions determined from the models produce values consistent with current technology devices (see Results section). Radiation calculations were validated by running a zero-thrust trajectory in a circular equatorial orbit within the Van Allen belts. Integration of the flux levels for the flight time compared with analytic calculations for this simple trajectory. A trivial case is run to check the validity of the radiation model. Results were also obtained for circular inclined orbits to assess radiation changes with latitude.[12]

Convergence studies were also performed for the fourth-order, fixed-step, Runge–Kutta time integration scheme. A step size was chosen for the three different types of trajectory: low-thrust, high-thrust, and coast phase. To determine the sensitivity of the solution to the step size, the same mission was run with three different low-thrust integration steps 1, 5, and 10 s. The results show that a step size of 5 s gives a solution insensitive to step size. Above 5 s, the solution changes and becomes less and less accurate until it diverges (around 60 s). A step size of 0.01 s was chosen for the high-thrust and coast phase. It gives an increment of 90 g of propellant expended each time step during engine burns. This increment is small enough to allow a smooth integration of the equations of motion. Moreover, the step size is suitable to satisfy the switch condition for the second burn during the coast phase, that is, flight-path angle less than 10^{-3} deg.

Results

A parametric study is performed on four variables: the altitude/radius of the first high-thrust burn (R_{switch}), the payload mass, the low-thrust engine type, and the inclination. The effect on the total trip time, the spacecraft's gross weight, and the radiation level are all quantified. For each run, TB1 ranges from 0 to 150 s. A value of TB1 of zero corresponds to the low-thrust case (L). Consequently, for this first run, the high-thrust inert mass is not included in the propulsion mass budget. The high-thrust case (H) is run separately, and the results are recorded in a table for later comparison.

Baseline Case

Table 3 highlights inputs assumed for a baseline case employing an L/H/L strategy used in most of the studies. For this case, a more detailed trajectory analysis and overall performance are presented. Also, a complete mass budget and propulsion sizing is provided for a chosen mission (TB1 = 75 s).

The baseline study demonstrates the efficiency of the TB2 algorithm in providing a nearly circular orbit at arrival. The eccentricity of the high-thrust transfer varies from 0 to 0.25 with TB1. After the second burn, for TB1 = 150 s, an eccentricity of 0.013 is observed. The final eccentricity ranges from 0.0011 to 0.0017, which is close to the desired circular orbit.

Gross Weight/Time of Flight/Radiation Exposure for Baseline Case

Figure 5 summarizes results for the baseline case for a family of vehicles spanning an all low-thrust (L) to an all high-thrust (H) mission strategy. Results are summarized in terms of the first burn of the high-thrust system. The time of flight decreases as the chemical propulsion portion of the mission is increased with TB1. As mentioned earlier, this paper focuses on obtaining general trends for different engine power. No intent was made to match specific engine weights. Thus, in an attempt to keep the study generic, analytical equations were used and, in some cases, lead to significant difference with actual thruster weight.

Table 3 Baseline case parameters

Parameter	Value
Low-thrust engine	HET-220
Inclination	0 deg
Payload mass	750 kg
Switch radius	7000 km

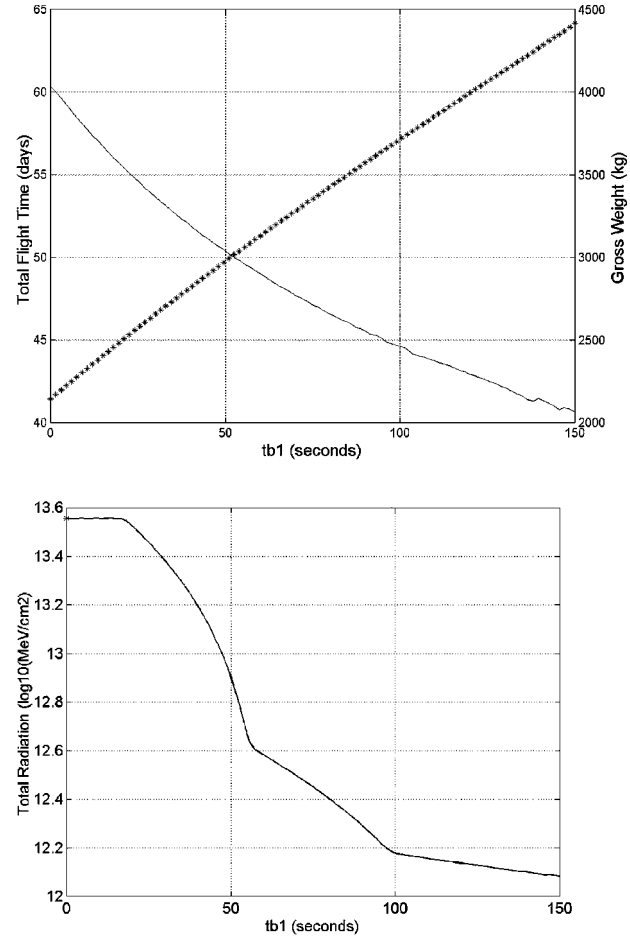

Fig. 5 Variation of total flight time (days), gross mass (kilograms) and radiation dosage (megaelectron volts per square centimeter) with TB1 (HET-220 engine, $M_{\text{pl}} = 750$ kg, inclination = 0 deg and $R_{\text{switch}} = 7000$ km).

Without including any high-thrust system, the four HET-220 engines give a fairly decent trip time (about 60 days). For a maximum of TB1 = 150 s, the trip time has reduced to roughly 40 days. As observed in Fig. 5, this reduction in trip time is accompanied by a 100% increase in gross weight. The efficiency of the high thrust to reduce the radiation dosage is divided in four zones. Note that radiation doses are expressed logarithmically. From $0 < \text{TB1} < 20$ s the radiation remains essentially constant because the high-thrust system does not boost the vehicle through a significant portion of the Van Allen belts. For $20 < \text{TB1} < 55$ s, the radiation dose decreases from 3.7×10^{13} to 0.4×10^{13} MeV/cm^2, which represents a 90% change. In this range, the high-thrust system is providing transit across the main damaging radiation zone located between 1.2 and 1.4 Earth radii. For $55 < \text{TB1} < 100$ s, a small improvement is still observed as the outer radiation belt is traversed. Beyond 100 s, only a minor reduction in total radiation flux is realized.

The lowest radiation level is obtained using the high-thrust case, which then gives a radiation dosage of 3.12×10^{10} MeV/cm^2. The total radiation obtained with this case is 40 times smaller than the dosage recorded at TB1 = 150 s for the L/H/L case. The high thrust gives a lower bound to the radiation dose. However, it is difficult to judge whether the radiation level for TB1 = 150 s is adequate in terms of damage to the system. A more in depth study would be needed to determine the maximum acceptable level of radiation on the spacecraft. In fact, this is still a topic of debate in the industry; the intent here is to assess the sensitivity of the total dose to the propulsion system and trajectory choice.

Mass Budget and Propulsion Sizing

Table 4 summarizes the mass budget of the high-thrust and low-thrust propulsion systems for the baseline case at TB1 = 75 s.

Table 4 Mass summary for 750-kg payload

Variable	Mass, kg
High-thrust propulsion system	
Oxidizer (N_2O_4)	424.9
Fuel (MMH)	701.1
Oxidizer tank	29.3
Fuel tank	29
Pressurant	8.3
Pressurant tank	75
Combustion chamber/injector	1.9
Nozzle	13.6
Margin (5%)	56.3
Low-thrust propulsion system	
Propellant (xenon)	355.4
Propellant tank	23.1
Thrusters/PPU	475.5
Radiators	85
Solar arrays	308.2
Margin (5%)	17.8

Table 5 Performance summary for 750-kg payload

Variable	Value
High-thrust propulsion system	
Tank pressure, MPa	1.08
Tank burst pressure, MPa	1.35
Pressurization tank pressure, MPa	21.
Combustion chamber pressure, MPa	0.862
Combustion chamber burst pressure, MPa	2.69
Thrust, N	26,700
Specific impulse, s	313.2
Thrust coefficient	1.85
Contraction area ratio	2.85
Expansion area ratio	25
Low-thrust propulsion system	
Tank pressure, MPa	24
Tank burst pressure, MPa	30
Thrust, mN	524
Specific impulse, s	2,379
Power, kW	43
Thruster efficiency, %	53

Propellant masses, solar arrays, and power conditioning masses dominate the overall mass budget. The inert mass of the chemical propulsion system is dominated by the pressurant and pressurant tank. Note that the nozzle and combustion chamber/injector subsystems have a fixed mass of 15.5 kg. The electric propulsion system inert mass is dominated by the thruster and PPU, which accounts for 52% of the inert mass of the system. Because of the very high power levels required for processing of the four HET-220 thrusters selected for this mission, significant extrapolation from the database used to develop the constants C and D in Eq. (1) is required for this vehicle. The solar arrays comprise 34% of the inert mass of the low-thrust system, whereas propellant tanks account for only 3% of the total budget. Because the electric propulsion system is sized almost entirely by the input power, inert mass is nearly independent of the propellant mass. Therefore, for a given low-thrust engine, the low-thrust inert mass is unlikely to change significantly for the different missions studied. For this particular design, the 750-kg payload mass represents roughly 22% of the vehicle gross weight.

Tables 5 and 6 present performance and dimensional summaries for this baseline case. Tank and chamber pressures were chosen to be consistent with current technology propulsion systems. Contraction and nozzle half-angles represent the nozzle entry and exit angles with respect to the centerline of the engine. Note that the 43-kW power required for operation of the thruster bank necessitates large solar arrays and would represent a substantial increase over currently demonstrated power levels achieved for spacecraft.

The 37.5-m wing length represents a challenge for array designers. Figure 6 presents a to scale schematic of the vehicle excluding payload elements such as antennas and outer portions of the array.

Table 6 Dimensional summary

Variable	Value
Oxidizer tank radius, m	0.503
Fuel tank radius, m	0.501
Pressurization tank radius, m	0.376
Combustion chamber radius, m	0.123
Contraction half-angle, deg	45
Combustion chamber length, m	0.268
Throat radius, m	0.0729
Exit radius, m	0.365
Nozzle length, m	1.09
Nozzle half-angle, deg	15
x_e Tank radius, m	0.323
Solar array length (one wing), m	37.5
Solar array height (one wing), m	4

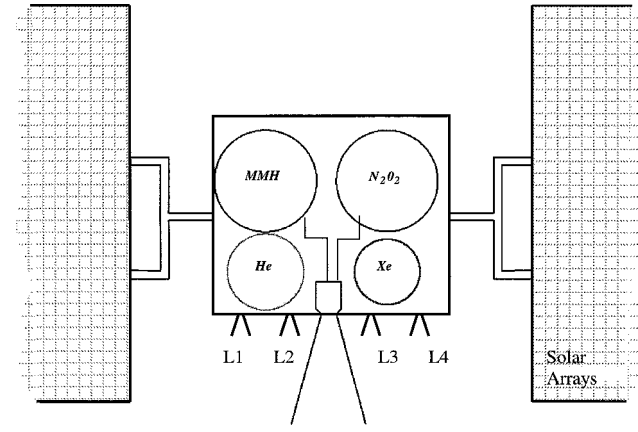

Fig. 6 Scale schematic of the baseline vehicle designed for TB1 = 75 s; low-thrust engine: HET-220, inclination = 0 deg, payload mass = 750 kg, and R_{switch} = 7000 km.

Orbit Description and Performance

The five phases of a general transfer mission are noted in Fig. 3. The major part of the mission is spent in the last phase, corresponding to about 88% of the total trip time for the baseline case at TB1 = 75 s (150 revolutions). The first low-thrust phase represents 11% of the time of flight (69 revolutions). The remainder is the time is spent during the coast phase. The radiation dosage is the most significant during the last low-thrust phase. This is not surprising because it is during this period that the spacecraft spends the major part of its trip, a portion of which is in the upper portion of the Van Allen belts for this baseline case with TB1 = 75 s. No radiation is observed during the first phase because at the altitude and inclination flown, the radiation levels are negligible during this portion of the trajectory. For the electric propulsion system, the thrust-to-weight ratio starts as low as 6.23×10^{-5} and reaches its highest value at the end of the mission with 1.26×10^{-4}. For the chemical propulsion system, the same parameter varies from 0.82 for the first burn to 1.02 for the second burn. The low-thrust trajectory flight-path angle and eccentricity are small (see Fig. 3). The Hohmann transfer eccentricity is about 0.15, and its maximum flight-path angle is about 9 deg.

Influence of the Switch Radius

The first high-thrust burn was performed at four different radii (R_{switch}): 6578; 7000 (baseline case); 9000; and 10,000 km. The R_{switch} case of 6578 km represents the initial LEO orbit assumed and, therefore, represents a case where no electric propulsion is used before chemical propulsive burns (H/L case). In many respects, this architecture is the most sensible because it would not necessitate a deploy/storage/deploy scenario for the solar arrays. Over the R_{switch} range considered, the switch radius has little influence on the gross weight. The major change is an increase in the low-thrust propellant mass because the first phase lasts longer for a higher switch radius. For a TB1 of 150 s, the gross weight is roughly 5% larger for a switch radius of 9000 and 10,000 km than for a switch radius of 6578 and 7000 km.

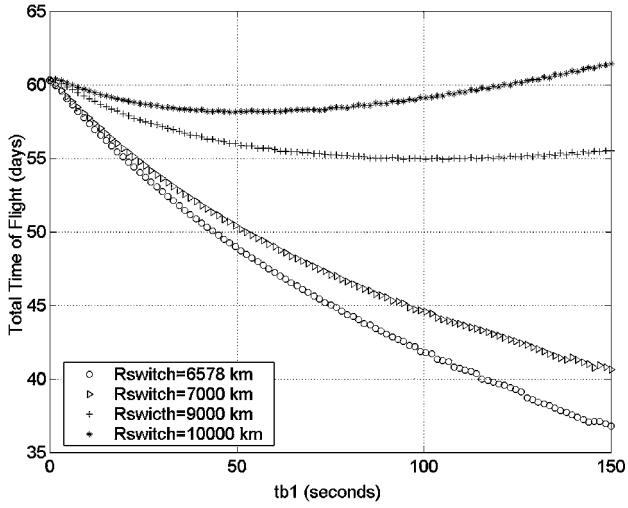

Fig. 7 Time of flight (days) for different switch radii (HET-220 engine, $M_{pl} = 750$ kg, and inclination = 0 deg).

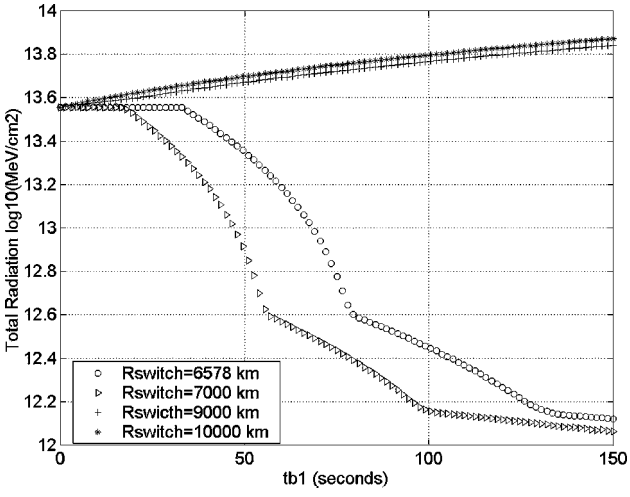

Fig. 8 Radiation dosage (megaelectron volts per square centimeter) for different switch radius (HET-220 engine, $M_{pl} = 750$ kg, and inclination = 0 deg).

The total trip behavior is shown in Fig. 7. The H/L case presents the lowest trip time. The high-thrust phase occurs at the very beginning of the mission and the high-thrust inert mass is dropped just after the first phase. As R_{switch} grows, the time spent in the first low-thrust phase increases, leading to a longer time of flight. Note that there is an optimum value of TB1 (about 50 s for $R_{switch} = 10{,}000$ km and about 100 s for $R_{switch} = 9000$ km). Beyond this optimum, the time of flight increases, although more energy is given to the system. This effect is attributed to the growth in vehicle mass attendant with the increased use of the chemical propulsion system, that is, even though more velocity increment is imparted by the chemical stage, the first low-thrust burn is impacted by the heavier vehicle during this segment. For a switch radius of 10,000 km, the trip time of the L/H/L case at TB1 = 150 s is higher than the L case. Therefore, the gross weight increase does not have a great impact on the trip time as long as the Hohmann transfer is performed close enough to the departure orbit.

The influence of the switch radius on radiation exposure is presented in Fig. 8. The high-thrust system is completely ineffective in reducing radiation exposure for an R_{switch} of 9000 and 10,000 km. This was expected because the first low-thrust phase occurs in the high-energy radiation zone, and the time spent in this zone increases as the vehicle gets heavier. For a given TB1, the high-thrust phase effectiveness in reducing radiation dosage is delayed for the H/L case as compared to the baseline case. The altitude reached after a first burn time of 50 s is lower because the mission started at 6578 km instead of 7000 km. Thus, it needs more energy to cross the high-energy radiation zone. Consequently, the L/H/L strategy is preferred to minimize radiation exposure.

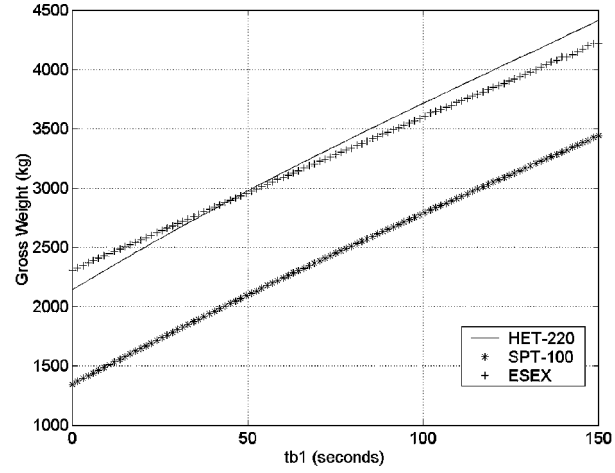

Fig. 9 Vehicle gross weight changes with varying amounts of chemical propulsion: effects of electric propulsion engine ($M_{pl} = 750$ kg, inclination = 0 deg, and $R_{switch} = 7000$ km).

Influence of the Electric Propulsion Engine

Three electric propulsion engines are studied: HET-220, SPT-100, and ESEX. Note that the four HET-220 have approximately the same thrust level as the ESEX (about 2 N). The four SPT-100 supply a much lower thrust level of about 0.33 N, which represents one-sixth of the ESEX engine thrust.

Figure 9 provides a gross weight comparison for vehicles based on the three engines for the conditions noted in the baseline case in Table 3. The SPT-100 system gross weight is the lowest because its power consumption, inert mass, and propellant consumption are the lowest. The HET-220 system provides a lower gross weight than the ESEX-based vehicle for a TB1 smaller than 50 s. For small TB1, more low-thrust propellant is required and the arcjet engine consumes about 2.6 times more propellant than the HET-220 system. However, the ESEX-based vehicle has an inert mass 2.25 times lower than the HET-220 due to the lower power requirement (26 vs 43 kW for the HET-220 system). As high-thrust energy is added, the low-thrust propellant mass decreases. Thus, the inert mass becomes a more dominant parameter and, for TB1 higher than 50 s, the HET-220 gross weight exceeds the ESEX-based vehicle.

The four SPT-100 design reaches GEO in about 220 days for the all-electric L strategy and in about 125 days for a TB1 of 150 s. This trip time is not appealing for commercial applications, which generally desire a maximum of 90 days. The HET-220 and ESEX are in the same order of time of flight (about 60 days maximum) with a slightly better result with the ESEX (about 5 days shorter). Again, this can be explained by the difference in inert mass between the two engines.

The HET-220 and ESEX-based vehicles exhibit about the same radiation damage. As expected, the radiation damage is the most important when using the SPT-100 with a radiation of about 14×10^{13} MeV/cm^2 for the L case (Fig. 10). This is 3.5 times higher than the ESEX and HET-220. There is a small region in the design space near TB1 = 35 s where the SPT-100 system actually provides the lowest dosage. This interesting result occurs because the SPT-100 vehicle is inherently lighter than the other two alternatives, and, with a modest amount of chemical propulsion, a large extent of the radiation zones can be traversed. At higher TB1 values, the heavier ESEX and HET-220-based vehicles are able to traverse the highest radiation zones, and overall trip time effects become more important. In this high-radiation region, the SPT-100 system has the highest radiation dosage.

Influence of Payload Mass

To assess the influence of the payload masses on the results, the code was run for three different payload masses: 500, 750, and

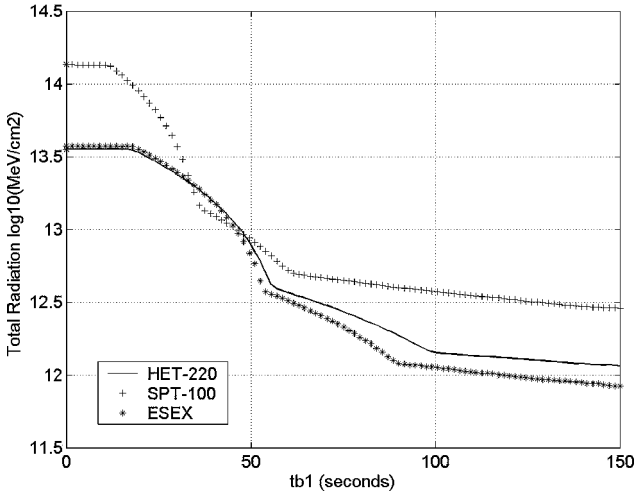

Fig. 10 Radiation dosage (megaelectron volts per square centimeter) for different low-thrust engines (M_{pl} = 750 kg, inclination = 0 deg, and R_{switch} = 7000 km).

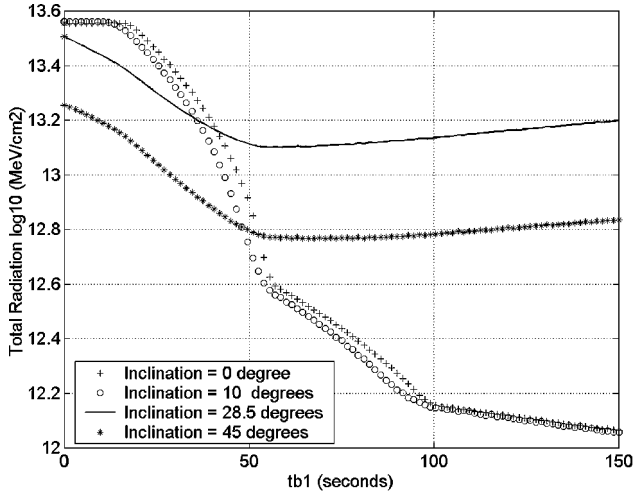

Fig. 11 Radiation dosage (megaelectron volts per square centimeter) at different inclinations vs TB1 (HET-220 engine, M_{pl} = 750 kg, R_{switch} = 7000 km).

1000 kg for the other baseline cases noted in Table 3. Essentially linear results were obtained for these cases, with gross weight, trip time, and radiation dosage all scaling directly with payload mass.[12] A change in payload mass of 250 kg leads to a change in gross weight of about 350 kg. The trip time increases about 9.5 days for the L case and about 8 days for an L/H/L with a TB1 of 150 s per 250-kg increase in payload mass. An increment of 0.55×10^{13} MeV/cm^2 was computed as the payload mass increased by 250 kg. Also, as the spacecraft carries more payload, more high-thrust energy (about 8 s in TB1) is required to obtain the same efficiency in decreasing the radiation level. Note that the minimum radiation exposure (about 3×10^{10} MeV/cm^2) is obtained with the H case. The damage increases slightly with the payload mass. However, the H case exhibits a very high gross weight that varies greatly with the payload mass between 5000 for a payload mass of 500 and 10,500 kg for a 1000-kg payload mass.

Influence of Inclination Angle

The inclination only affects the radiation level because the trajectory is assumed to be coplanar in this study. However, a transfer from LEO to GEO requires a plane change from an inclination of 28.5 deg to an inclination of 0 deg if one assumes a coplanar launch from NASA Kennedy Space Center. Thus, the influence of four different inclinations is studied (0, 10, 28.5, and 45 deg). Other conditions were consistent with those in the baseline case noted in Table 3. Results in Fig. 11 indicate that an inclination of 10 deg is small enough to produce a radiation history almost identical to the baseline case with 0 deg of inclination. The high-thrust efficiency in reducing the radiation dosage is better than the baseline case for TB1 > 50 s due to the torroidal shape of the zone being crossed. This effect tends to be more pronounced at the higher inclinations; recall that the radiation belts are mainly confined to inclinations below 60 deg, and so higher inclinations intercept an ever-decreasing slice of the zone. Consequently, a coplanar transfer is reasonable for predicting radiation damage because most of the plane change typically occurs outside the radiation zone.

Inclinations of 28.5 and 45 deg exhibit a radiation profile different from the baseline. The high-thrust transfer reduces the radiation level until it reaches an optimum value (TB1 of about 50 s). Beyond this optimum, the radiation damage rises again. There are several reasons that explain this behavior. For a circular trajectory at $R = 7000$ km, the L-shell value is influenced by the inclination. The L-shell value oscillates more as the inclination gets bigger [see Eq. (2)]. For an inclination of 28.5 deg, the vehicle flies about 40% of its circular period in the highest radiation zone, although, for the baseline case, the orbit does not enter this highest energy off-axis region. The switch between radiation zones tends in general to be an advantage for the radiation dosage except for the first low-thrust phase in the L/H/L strategy. For small inclinations, this phase of the mission stays out of the high-radiation energy zone. For the baseline case, the main damage is due to the last low-thrust phase. There is no damage during the first low-thrust phase and the high-energy zone is crossed using the high-thrust propulsion. The damage during the coast phase is also negligible due to its relatively short time of flight. However, for higher inclinations, the L-shell value increases and a portion of the trajectory in phase 1 is subject to high-radiation damage. Thus, the time of flight, which had not had an effect on the radiation level before, now plays an important role.

Conclusions

A hybrid orbital transfer that employs both low-thrust electric propulsion and high-thrust chemical propulsion has been evaluated. The high-thrust system has been shown effective in reducing trip time and radiation damage in the Van Allen belts, whereas the efficiency of the low-thrust system provides for dramatic reductions in vehicle gross weights. Both H/L (high-thrust followed by low-thrust phase) and L/H/L strategies were studied; the latter strategy is employed to provide efficient transit to the lower edge of the high-radiation zones. The L/H/L strategy was proven to be more efficient than the H/L strategy, although this approach would necessitate a deploy/storage/deploy strategy for solar arrays.

Depending on the relative amounts of chemical propulsion employed, radiation exposures can be reduced by a factor of 10–50 compared to an all electric propulsion vehicle over the parameter range studied. The baseline switch radius of 7000 km appears a reasonable choice for an equatorial plane change in providing the benefits of electric propulsion before entry to high-radiation zones. However, a slightly higher or lower value can result, depending on the inclination of the initial orbit.

Among the three electric propulsion engines studied, the SPT-100 is the most attractive in terms of reducing vehicle gross weight at the expense of slightly higher trip times and radiation exposures. In spite of its inferior specific impulse, the ESEX engine provided competitive designs due to the reduced power requirement as compared to the other vehicles studied. To obtain trip times less than one year, four engine clusters of the HET-220 and SPT-100 engines were required to boost payloads in the 500–1000-kg range. As a result, vehicles based on these systems have more demanding power requirements. The inclination has a complex and significant influence on the radiation damage. Because of the torroidal shape of the Van Allen belts, the highest radiation was noted at a 28.5-deg inclination for vehicles using modest to high amounts of high-thrust propulsion. For vehicles using lower amounts of chemical propulsion, low-inclination trajectories provided the highest damage.

References

[1]Martinez-Sanchez, M., and Pollard, J. E., "Spacecraft Electric Propulsion: An Overview," *Journal of Propulsion and Power*, Vol. 14, No. 5, 1998, pp. 688–699.

[2]Bennett, G. L., Brandhorst, H. W., Bankston, C. P., and Sovie, R. J., "Electric Power System Development: A Companion Technology to Electric Propulsion," AIAA Paper 97-2784, July 1997.

[3]Spencer, D., and Culp, R., "Designing Continuous Low-Earth-Orbit to Geosynchronous-Earth-Orbit Transfers," *Journal of Spacecraft and Rockets*, Vol. 32, No. 6, 1995, pp. 1033–1038.

[4]Kechichian, A., "Optimal Low-Earth-Orbit-Geostationary Orbit Intermediate Acceleration Orbit Transfer," *Journal of Guidance, Control, and Dynamics*, Vol. 20, No. 4, 1997, pp. 803–811.

[5]Scheel, W., and Conway, B., "Optimization of Very-Low Thrust, Many Revolution Spacecraft Trajectories," *Journal of Guidance, Control, and Dynamics*, Vol. 17, No. 6, 1994, pp. 1185–1192.

[6]Kluever, C., and Oleson, R., "Direct Approach for Computing Near-Optimal Low-Thrust Earth-Orbit Transfers," *Journal of Spacecraft and Rockets*, Vol. 35, No. 4, 1998, pp. 509–515.

[7]Kechichian, A., "Reformulation of Edelbaum's Low-Thrust Transfer Problem Using Optimal Control Theory," *Journal of Guidance, Control, and Dynamics*, Vol. 20, No. 5, 1997, pp. 988–994.

[8]Matogawa, Y., "Optimum Low Thrust Transfer to Geosynchronous Orbit," *Acta Astronautica*, Vol. 10, No. 7, 1983, pp. 467–478.

[9]Edelbaum, T. N., "The Use of High- and Low-Thrust Propulsion in Combination for Space Missions," *Journal of the Astronautical Sciences*, Vol. 9, No. 2, 1962, pp. 49–69.

[10]Kluever, C., "Spacecraft Optimization with Combined Chemical–Electric Propulsion," *Journal of Spacecraft and Rockets*, Vol. 32, No. 2, 1994, pp. 378–380.

[11]Kluever, C., "Optimal Earth–Moon Trajectories Using Combined Chemical–Electric Propulsion," *Journal of Guidance, Control, and Dynamics*, Vol. 20, No. 2, 1997, pp. 253–258.

[12]Mailhe, L. M., "Design of a High Thrust/Low Thrust Orbital Transfer Vehicle Considering Van Allen Radiation Belts," M.S. Thesis, School of Aeronautics and Astronautics, Purdue Univ., West Lafayette, IN, Aug. 1999.

[13]Teague, C. E., "OMS Engine Flight Report STS-1 and 2," AIAA Paper 82-1104, June 1982.

[14]Humble, R. W., Henry, G. N., and Larson, W. L., "Space Propulsion Analysis and Design," *Space Technology Series*, 1st ed., McGraw–Hill, New York, 1995, Chaps. 5, 9.

[15]Lee, J. C., and Ramirez, P., "Pressurization Systems for Liquids Rockets," NASA SP-8112, 1975.

[16]Bromaghim, D. R., and Sutton, A. M., "Electric Propulsion Space Experiment Integration and Test Activities on the Advanced Research and Global Observation Satellite," AIAA Paper 96-2726, July 1996.

[17]Kozubsky, K. N., Kim, V., Colbert, T. S., Day, M., Fisher, G., Randolph, T. M., and Rogers, W. P., "Plan and Status of the Development and Qualification Program for the Stationary Plasma Thruster," AIAA Paper 93-1787, June 1993.

[18]Jandovsky, R. S., and McLean, C., "Preliminary Evaluation of a 10-kW Hall Thruster," AIAA Paper 99-0456, Jan. 1999.

[19]Larson, W. L., and Wertz, J. R., *Space Mission Analysis and Design*, 2nd ed., Kluwer Academic and Microcosm, Norwell, MA, 1992, Chap. 8.

[20]LeMaire, J. F., Heyndrickx, D., and Baker, D. K. (eds.), "Radiation Belts: Models and Standards," American Geophysical Union, Geophysical Monograph 97, 1996.

[21]Vaughn, E., and Cassady, J., "Updated Assessment of Electric Propulsion Technology for Near-Earth Space Missions," AIAA Paper 92-3202, July 1992.

[22]Vette, J. I., Lucero, A. B., and Wright, J. A., "Models of the Trapped Radiation Environment, Vol. II: Inner and Outer Zone Electrons," NASA SP-3024, 1966.

[23]Daly, E. J., Lemaire, J., Heynderickx, D., and Rodgers, D. J., "Problems with Models of the Radiation Belts," *IEEE Transactions on Nuclear Science*, Vol. 43, No. 2, 1996, pp. 403–415.

[24]Janssens, F., and Dutruel-Lecohier, G., "Introduction to Low-Thrust Transfers to the Moon," European Space Research and Technology Center, Working Paper 1948, Aug. 1997.

[25]Chobotov, V., *Orbital Mechanics*, 2nd ed., edited by J. S. Przemieniecki, AIAA, Reston, VA, 1996, Chap. 6.

D. L. Cooke
Associate Editor